



CHORUS

This is the accepted manuscript made available via CHORUS. The article has been published as:

Bayesian reconstruction of gravitational wave bursts using chirplets

Margaret Millhouse, Neil J. Cornish, and Tyson Littenberg

Phys. Rev. D **97**, 104057 — Published 29 May 2018

DOI: [10.1103/PhysRevD.97.104057](https://doi.org/10.1103/PhysRevD.97.104057)

Bayesian reconstruction of gravitational wave bursts using chirplets

Margaret Millhouse and Neil J. Cornish

*eXtreme Gravity Institute, Department of Physics,
Montana State University, Bozeman, MT 59717, USA*

Tyson Littenberg

NASA Marshall Space Flight Center, Huntsville AL 35812, USA

Abstract

The LIGO-Virgo collaboration uses a variety of techniques to detect and characterize gravitational waves. One approach is to use templates - models for the signals derived from Einstein's equations. Another approach is to extract the signals directly from the coherent response of the detectors in LIGO-Virgo network. Both approaches played an important role in the first gravitational wave detections. Here we extend the `BayesWave` analysis algorithm, which reconstructs gravitational wave signals using a collection of continuous wavelets, to use a generalized wavelet family, known as chirplets, that have time-evolving frequency content. Since generic gravitational wave signals have frequency content that evolves in time, a collection of chirplets provides a more compact representation of the signal, resulting in more accurate waveform reconstructions, especially for low signal-to-noise events, and events that occupy a large time-frequency volume.

I. INTRODUCTION

The first gravitational wave signal recorded by the advanced LIGO detectors [1], GW150914, was detected by multiple search pipelines [2], some that directly reconstruct the signal using a coherent wavelet representation [3], and others that use waveform models, or templates, derived from general relativity [4]. Both types of analysis play an important role in gravitational wave (GW) detection and characterization: the modeled searches are the most sensitive to the types of signals they are targeting, while the direct reconstruction methods are sensitive to a wider variety of GW sources. Both types of analysis also play an important role in understanding the physical properties of the sources. The template based analysis provides a mapping between the shape of the waveform and the physical properties of the source, allowing us to infer that GW150914 was produced by the collision of two black holes, each ~ 30 times the mass of the Sun [5]. The greater flexibility of the wavelet-based reconstruction approach was used to test for deviations from the predictions of general relativity by using `BayesWave` to search for excess power that was not picked up by the templated reconstructions [6].

While all of the GWs detected so far have been from compact binary systems, there exist other GW sources that are not as well modeled: for example core-collapse supernovae; post-merger oscillations of hypermassive neutron stars; magnetar flares; and pulsar glitches. There is also the possibility that LIGO/Virgo could detect gravitational waves from a completely new and unpredicted sources. In addition to having good models for well understood sources, it is also crucial that we are ready to both detect and characterize any possible astrophysical signal.

One analysis technique that has been widely used in LIGO to detect and reconstruct GWs with minimal assumptions is the `BayesWave` algorithm [7]. Several studies [8–10] have shown `BayesWave`'s capability to robustly distinguish between real astrophysical signals and transient noise artifacts (glitches) that are known to occur in the detectors, and to faithfully reconstruct waveforms from simulated signals. It does this by reconstructing the detector data using a sum of Morlet-Gabor sine-Gaussian wavelets. The number of wavelets used is determined by the data, with more complicated signals (*i.e.* those having more structure in time-frequency space) needing more wavelets. Because Morlet-Gabor wavelets have variable shapes in time-frequency space they are generally able to fit waveforms well, but there are

several avenues for improving the fidelity of the waveform reconstructions. One is to modify the prior on the wavelet placement - such as using a “clustering prior” [7] which assigns greater probability to regions in time-frequency that are close to other wavelets. Another is to change the wavelet model. Here we investigate the use of “chirplets” - modified sine-Gaussian wavelets with linear frequency evolution [11]. The motivation for using chirplets is that the frequency content of GW signals typically evolves with time [12–16]. The chirplets can model both increasing and decreasing frequency evolution.

II. CHIRPLET FRAME

The Morlet-Gabor sine-Gaussian wavelets currently used by `BayesWave` form an over-complete basis, technically a *frame* [17], that can reconstruct any possible signal. They have a simple analytic representation in the Fourier domain, making it easy to search over the time of arrival, and allowing for efficient calculation of the likelihood function. But there may be other frames that are able to reconstruct signals more efficiently.

In choosing a new wavelet frame for `BayesWave`, we consider what types of gravitational-wave signals we might detect. Many astrophysical sources of GWs have frequency content that evolves in time, most notably mergers of compact binary objects. Because of this, we might expect that using a frame function that itself includes frequency evolution could better reconstruct GW signals. The simplest way to incorporate changing frequency into `BayesWave` is to add a linear frequency evolution to the Morlet-Gabor wavelets, producing a function known as a chirplet [11].

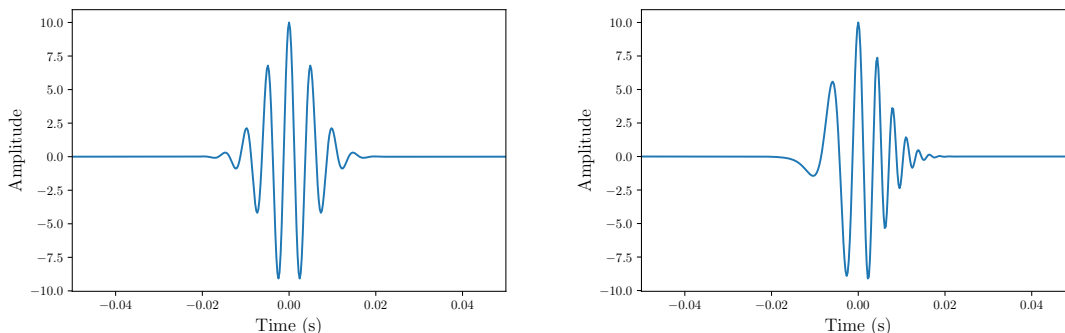


FIG. 1. Examples of a wavelet (left) and chirplet (right) in the time domain. For both examples $f_0 = 200$ Hz, $t_0 = 0$ s, $Q = 10$, $\phi_0 = 0$, and $A = 10$. In the chirplet example $\dot{f}_0 = 3158$ Hz².

In the time domain, chirplets can be expressed as

$$\Psi(t; A, f_0, \dot{f}_0, Q, t_0, \phi_0) = A e^{-\Delta t^2/\tau^2} \cos(2\pi f_0 \Delta t + \pi \dot{f}_0 \Delta t^2 + \phi_0) \quad (1)$$

where $\tau = Q/(2\pi f_0)$ and $\Delta t = t - t_0$. Here \dot{f}_0 represents the frequency evolution and is the linear frequency derivative at time $t = t_0$. In the limit that $\dot{f}_0 = 0$, this expression reduces to the expression for Morlet-Gabor wavelets. Chirplets can have either $\dot{f}_0 > 0$ (chirping), or $\dot{f}_0 < 0$ (anti-chirping). Time domain plots of a chirplet with $\dot{f}_0 > 0$ and a Morlet-Gabor wavelet ($\dot{f}_0 = 0$) are shown in Figure 1.

The same characteristics that make Morlet-Gabor wavelets a good frame are also true for chirplets: they are continuous, occupy a small time-frequency volume, and can be expressed analytically in the Fourier domain, though with a slightly more complicated expression:

$$\begin{aligned} \Psi(f; A, f_0, \beta, Q, t_0, \phi_0) = & \frac{A\sqrt{\pi}\tau}{2(1 + \pi^2\beta^2)^{1/4}} e^{-\frac{\pi^2\tau^2\Delta f^2}{1+\pi^2\beta^2}} e^{-2\pi i f t_0} (e^{i(\phi_0 + \delta - \pi^3\beta\tau^2\Delta f^2)/(1+\pi^2\beta^2)} \\ & + e^{-Q^2 f/f_0} e^{-i(\phi_0 + \delta - \pi^3\beta^2\Delta f^2)/(1+\pi^2\beta^2)}) \end{aligned} \quad (2)$$

where $\Delta f = f - f_0$, $\delta = \frac{1}{2} \arctan(\pi \dot{f}_0 \tau^2)$, and we have introduced the dimensionless parameter $\beta = \dot{f}_0 \tau^2$. For the remainder of this paper we will use β as our chirp parameter.

In time-frequency space, wavelets can be represented by ellipses whose principle axes are aligned with the time and frequency axes. Similarly, chirplets can be represented by a tilted ellipse. The equation for the ellipse is

$$(1 + \pi^2\beta^2)x^2 + \pi^2y^2 - 2\pi^2\beta xy = 1 \quad (3)$$

where we have introduced the dimensionless variables $x = \Delta t/\tau$ and $y = \tau\Delta f$. Details of the derivation of this expression can be found in the Appendix.

In terms of these new coordinates, the ellipse is tilted with respect to the time axis by the angle

$$\theta = \frac{1}{2} \arctan\left(\frac{2\pi^2\beta}{\pi^2(1 - \beta^2) - 1}\right) \quad (4)$$

The ellipse has area $1 + \mathcal{O}(\beta^4)$. A spectrogram of a variety of chirplets is shown in Figure 2.

III. METHODS

Bayesian inference requires the specification of a likelihood and prior, and a method to compute the posterior distribution and model evidence. Since the replacement of sine-Gaussian wavelets by chirplets only adds one new parameter to the frame functions, the

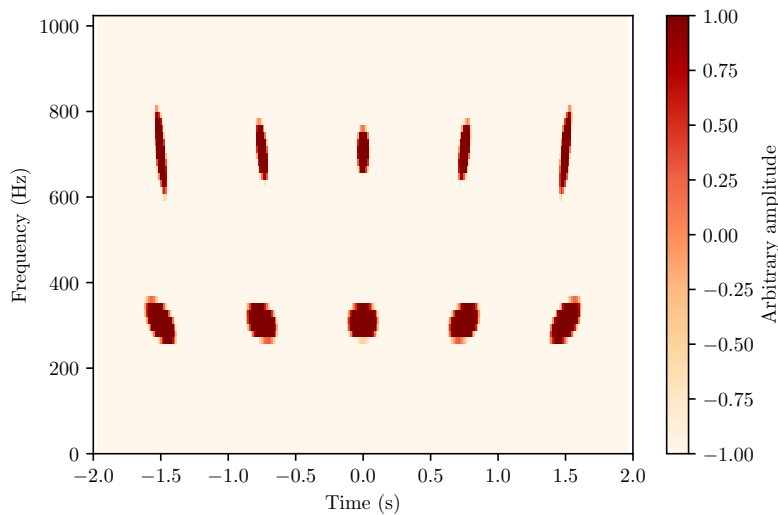


FIG. 2. Example spectrogram of chirplets at $f_0 = 300$ Hz, $Q = 100$ and $f_0 = 800$ Hz, $Q = 80$. For both frequency- Q combinations are shown chirplets with beta values of (from left to right) $\beta = -0.8, -0.4, 0.0, 0.4, 0.8$.

implementation is almost identical to the original `BayesWave` algorithm [7]. In our study we started with the version of `BayesWave` used in the second advanced LIGO observation run, which differs from the original in the choice of priors, and in some of the proposal distributions used to evolve the MCMC algorithm.

A. Priors and Proposals

We use uniform priors on Q ($Q \in [0.01, 40]$) and ϕ_0 ($\phi_0 \in [0, 2\pi]$). We also use a uniform prior on f_0 and t_0 over the time-frequency volume being analyzed.

The prior on the amplitudes of the individual wavelets (chirplets) is given as a prior on the SNR of the individual frame functions. For an individual wavelet or chirplet, the SNR is estimated as:

$$\text{SNR} \equiv 4 \int \frac{|\Psi(f; A, f_0, \dot{f}_0, Q, t_0, \phi_0)|^2}{S_n(f)} df \simeq \frac{A\sqrt{Q}}{\sqrt{2\sqrt{2\pi}f_0 S_n(f_0)}}, \quad (5)$$

where $S_n(f)$ is the one-sided power spectral density of the noise. The prior on the SNR for

wavelets in signal model is the same as described in Refs.[7, 8]:

$$p(\text{SNR}) = \frac{3\text{SNR}}{4\text{SNR}_*^2 \left(1 + \frac{\text{SNR}}{4\text{SNR}_*}\right)^5} \quad (6)$$

For the glitch model, the prior on the SNR is

$$p(\text{SNR}) = \frac{\text{SNR}}{2\text{SNR}_*^2 \left(1 + \frac{\text{SNR}}{2\text{SNR}_*}\right)^3} \quad (7)$$

where SNR_* is the SNR at which the distributions peak, empirically chosen to be $\text{SNR}_* = 5$.

For chirplets, we limited the tilt of the ellipse in τ -scaled time-frequency space to be below 45 degrees, which according to Eq. 4 corresponds to $\beta = \pm\sqrt{1 - 1/\pi^2} \approx \pm 0.95$. Physically this limit corresponds to roughly a doubling of the frequency across the duration of the chirplet. For larger values of $|\beta|$ the chirplets no longer provide a very compact time-frequency representation. We adopt a uniform prior on β in the range $\beta \in [-\sqrt{1 - 1/\pi^2}, \sqrt{1 - 1/\pi^2}]$. The prior on the number of frame functions is uniform in $N_w \in [0, 20]$.

For the jump proposals used in the RJMCMC, we follow the same proposals as described in [7]. One particular jump proposal is to use the Fisher information matrix, and update the frame function parameters by drawing from a multivariate Gaussian distribution defined by

$$q(\vec{x}|\vec{y}) = \frac{\sqrt{\det \Gamma}}{2\pi} e^{-\frac{1}{2}\Gamma_{ij}\Delta x^i\Delta x^j}. \quad (8)$$

The Fisher matrix for a single wavelet is given in [7], and we extend this Fisher matrix to a single chirplet. In the case the Fisher information matrix for a chirplet with parameters

$\vec{\theta} \rightarrow \{t_0, f_0, Q, \ln A, \phi_0, \beta\}$ is given by:

$$\Gamma = \text{SNR}^2 \begin{pmatrix} \frac{4\pi^2 f_0^2 (Q^2 + 1 + \pi^2 \beta^2)}{Q^2} & -2\pi^2 \beta & \frac{\pi^2 \beta f_0}{Q} & 0 & -2\pi f_0 & -\frac{\pi^2 f_0}{2} \\ -2\pi^2 \beta & \frac{Q^2 + 3 + 3\pi^2 \beta^2}{4f_0^2} & -\frac{3(1 + \pi^2 \beta^2)}{4Qf_0} & -\frac{1}{2f_0} & \frac{\pi\beta}{2f_0} & \frac{3\beta\pi^2}{8f_0} \\ \frac{\pi^2 \beta f_0}{Q} & -\frac{3(1 + \pi^2 \beta^2)}{4Qf_0} & \frac{3(1 + \pi^2 \beta^2)}{4Q^2} & \frac{1}{2Q} & -\frac{\pi\beta}{2Q} & -\frac{3\beta\pi^2}{8Q} \\ 0 & -\frac{1}{2f_0} & \frac{1}{2Q} & 1 & 0 & 0 \\ -2\pi f_0 & \frac{\pi\beta}{2f_0} & -\frac{\pi\beta}{2Q} & 0 & 1 & \frac{\pi}{4} \\ -\frac{\pi^2 f_0}{2} & \frac{3\beta\pi^2}{8f_0} & -\frac{3\beta\pi^2}{8Q} & 0 & \frac{\pi}{4} & \frac{3\pi^2}{16} \end{pmatrix}. \quad (9)$$

B. Simulated Data

To test the performance of the chirplet frame, we will look at how faithfully simulated GW signals can be reconstructed, and the number of frame functions used in the reconstruction. Our test data set consists of the of binary black hole merger signals, and unpolarized white noise bursts in simulated Gaussian noise at the aLIGO design sensitivity [18].

The binary black hole data set is a system of two $50M_\odot$ black holes with the waveform generated using the Effective One Body approximation [19] over a range of SNRs. We choose binary black holes as a test waveform in part because these are examples of waveforms we know have frequency evolution and thus are somewhere we believe a frame with frequency evolution could be beneficial. We also now know that GWs from black hole systems are detectable by LIGO, and we can likely expect more of these signals in the future. In addition to the standard BBH waveforms, we also tested BBH waveforms that have been time reversed, so that the frequency *decreases* over time. This set is used to demonstrate that the chirplet frame is good for general signals with time-frequency evolution, and is not specifically targeting BBH signals.

The second class of waveforms used are unpolarized white noise bursts (WNBs). These waveforms serve as a good test for the chirplet frame because they contain complicated frequency structure, which does not evolve smoothly like the BBH signals. These signals

can sometimes present challenges for `BayesWave` because they are unpolarized, whereas the current implementation of `BayesWave` assumes that the signals are elliptically polarized. We will see that this mis-modeling throws-off our estimates of the fidelity of the reconstruction as a function of signal-to-noise ratio. For this study we used WNB waveforms that had a characteristic duration of $\tau = 0.1$ s, and bandwidth of $\Delta f = 100$ Hz.

In previous studies of unmodeled searches [3, 20], sine-Gaussian waveforms (SGs) have also been used as test cases. However, we have already seen that though `BayesWave` can reconstruct SGs well, we are relatively insensitive to them in a search. This is a natural result of the fact that the signal-to-glitch Bayes factor scales with the number of wavelets used. For a sine-Gaussian signal we expect and indeed see that `BayesWave` typically uses only one wavelet to reconstruct SGs, so the Bayes factor scales only with SNR, making it more difficult to distinguish between signals and glitches. As wavelets are chirplets in the limit that $\dot{f}_0 \rightarrow 0$, we see the same behavior from chirplets and so do not consider SGs here.

IV. RESULTS

The two metrics we will look at are the number of frame functions used (N), and the match between waveforms, which as is defined as

$$M = \frac{(h|\bar{h})}{\sqrt{(h|h)(\bar{h}|\bar{h})}} \quad (10)$$

where \bar{h} is the injected signal, and h is the recovered signal, and $(a|b)$ denotes the standard noise-weighted inner product [21] evaluated across the detector network. Here we are using a simulated network consisting of the LIGO Hanford and Livingston observatories operating at design sensitivity.

A. Dimensionality

The results for the average (mean) number of frame functions and total dimensions used for the BBH injection set and the WNB injection set are shown in Figure 3. To find the total number of dimensions used, we multiply the number of frame functions used by five for wavelets and six for chirplets. The difference is more apparent for the BBH injections, but we see that in general fewer chirplets are used than wavelets. This is as predicted—

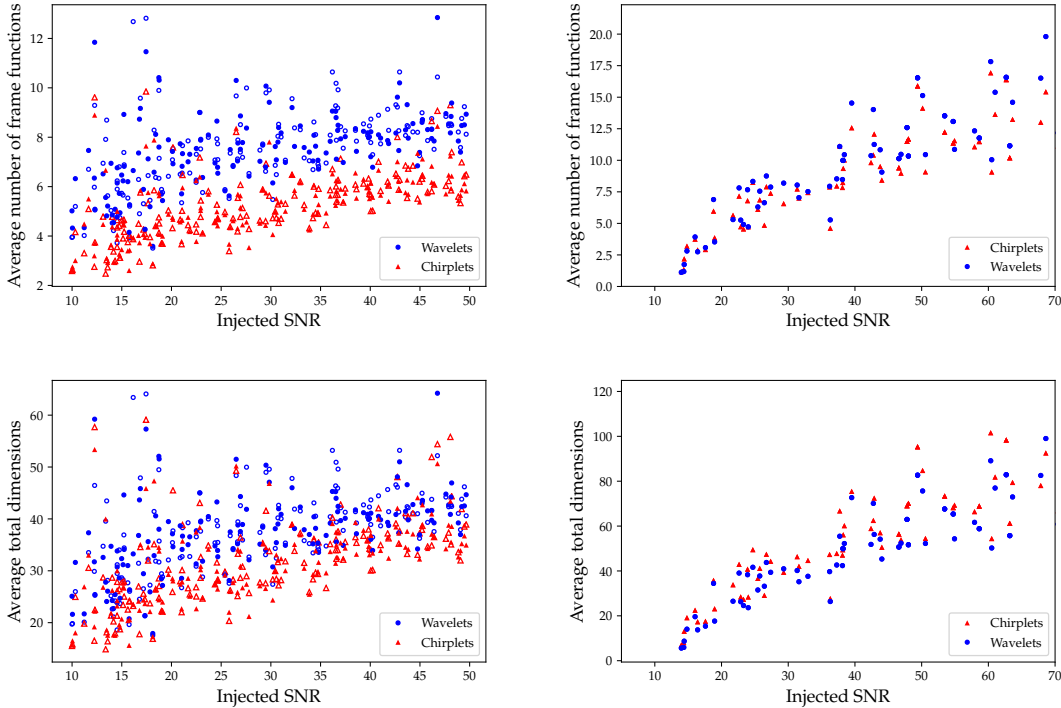


FIG. 3. The upper two panels show how the average number of frame functions (wavelets or chirplets) scales with the SNR. The lower two panels show the scaling for the total model dimension, which takes into account the number of parameters used by each frame function. The panels on the left are for $50M_{\odot}$ - $50M_{\odot}$ BBHs, and the panels on the right are for white noise bursts. The filled markers in the panels on the left represent regular BBH injections, and hollow marker represent time-reversed BBH injections.

the extra parameter, f_0 in the chirplet frame allows for fewer frame functions to be used in the reconstruction. For the BBH injections, we see that the chirplet frame function also uses fewer overall dimensions, while for the WNB injections though fewer chirplets are used the overall number of dimensions is slightly higher. This implies that the extra flexibility of chirplets may make them preferable for waveform reconstruction of BBH like events, particularly at low SNRs. A heuristic example of this can be seen in Fig. 4, where we see how the chirplets frequency evolution allows them to more closely follow the frequency evolution of the BBH signal.

We also see that, as shown in Ref. [8, 9], the number of wavelets used is roughly linearly dependent on the SNR of the injected signal. In Ref. [8] this dependence was written as

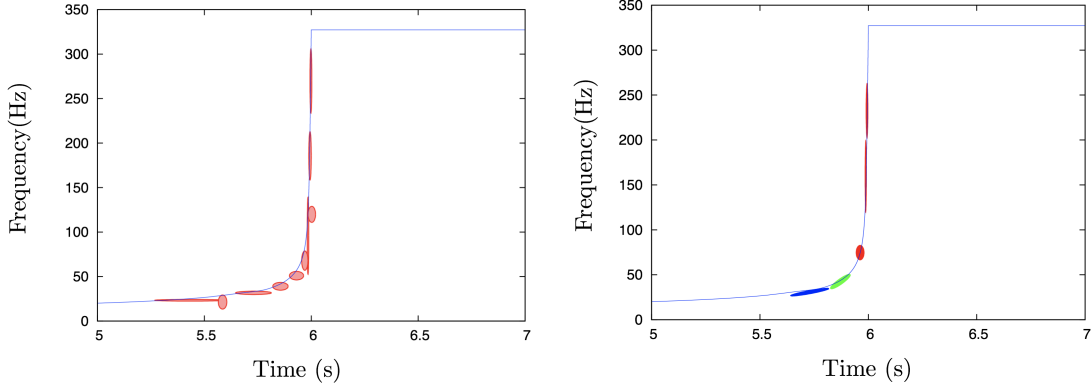


FIG. 4. An example of the wavelet frame (left) and chirplet frame (right) in action. In this case we used a simulated BBH signal with component masses of $29M_{\odot}$ and $30M_{\odot}$ at an SNR of 35. The solid line is the predicted $f(t)$ track and the colored ellipses are the wavelets or chirplets from a fair draw from the posterior distribution.

$N \approx 1 + \gamma \text{SNR}$, but here we generalize this expression to:

$$N \approx \alpha + \gamma \text{SNR}, \quad (11)$$

with the constants α and γ being determined by the waveform morphology. In practice this expression is only valid for sufficient large SNRs, otherwise the number of frame functions used drops rapidly to one (the minimum allowed number of frame functions in `BayesWave`'s signal model).

Using the results from the BBH injections, we perform a simple linear fit to find α and γ for the wavelet and chirplet runs. In both cases the slopes are very similar: $\gamma_{chirp} = 0.065$, $\gamma_{wave} = 0.066$. The starting number of frame functions though varies significantly: $\alpha_{wave} = 5.6$, and $\alpha_{chirp} = 3.3$. So while the number of frame functions used increases at a similar rate for both chirplets and wavelets, chirplets use reliably fewer frame functions.

For the WNB injections, we see that while for higher SNR injections slightly more wavelets tend to be used than chirplets, the difference is not nearly as striking as for BBH injections. Again with a simple linear fit we see $\gamma_{chirp} = 0.21$, $\gamma_{wave} = 0.23$, $\alpha_{chirp} = 0.76$, and $\alpha_{wave} = 0.53$, giving very similar slopes and starting points for both frame functions.

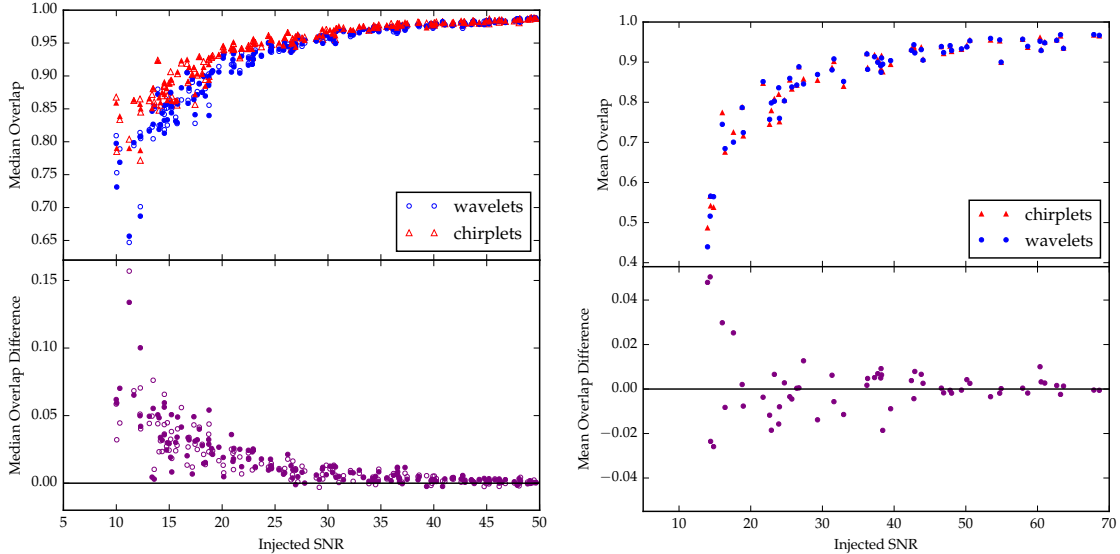


FIG. 5. The upper panels show the median match between the injected signal and reconstructed waveform versus SNR, while the lower panels shows the difference in the matches $\Delta M = M_{\text{chirplet}} - M_{\text{wavelet}}$. The plots on the left are for $50M_{\odot}$ - $50M_{\odot}$ BBH signals, while the plots on the right are for unpolarized white noise bursts.

B. Match

As predicted, the chirplet frame generally uses fewer frame functions. To test how well the injected signal is recovered, we look at the match. Fig. 5 shows the mean match between the injected and recovered waveforms for a set of two $50M_{\odot}$ BHs in simulated aLIGO noise (left) and a set of WNBs (right) for a range of SNRs using either chirplets or wavelets as the frame function.

In the BBH case, for SNRs above about 25, the matches of the two different methods are comparable. However at lower SNRs, we see that chirplets outperform wavelets, giving consistently higher matches. This is important because low SNR events are more common than high SNR events, so small improvements in performance for low SNR signals can result in a large number of additional detections. A particular example of a chirplet and wavelet reconstruction of a time-reversed BBH signal is shown in Fig. 6. The plots show the whitened strain, found by inverse Fourier transforming the Fourier domain signal $\tilde{h}(f)/\sqrt{S_n(f)}$. We see here that the chirplet frame manages to fit earlier and later parts of the signal.

For the WNB injections, we see that the two frame functions perform about equally as

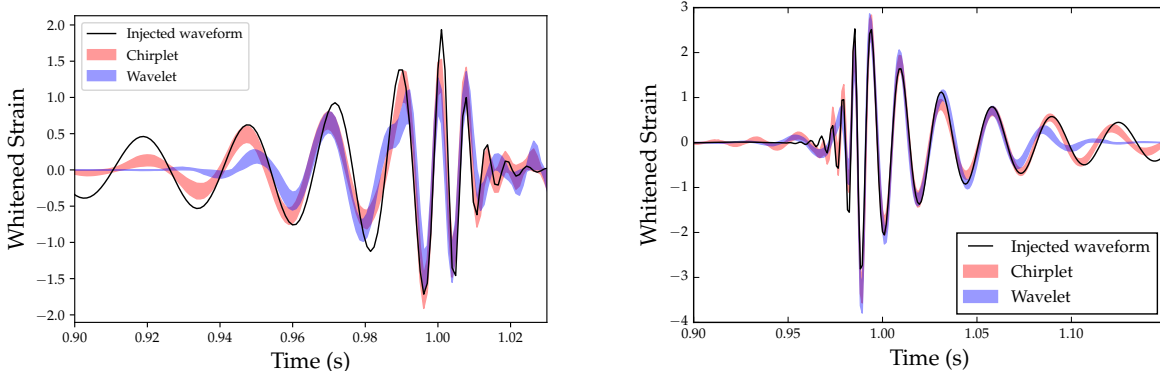


FIG. 6. Example of waveform reconstruction for a BBH, and a time reversed BBH system (both at $50\text{-}50M_{\odot}$). The red (blue) band shows the 50% credible interval of the reconstructed waveform using the chirplet (wavelet) frame. Both bases closely match the injected waveform (black) well in the higher power region, but chirplets are able to more accurately reconstruct the waveform in the regions with less power. The BBH event was injected with SNR 11.2, and has a median match of 0.79 for the chirplet frame, and 0.66 for the wavelet frame. The time-reversed BBH event was injected with a network SNR of 10.25. The median network match for the chirplet frame is 0.91, and for the wavelet frame it is 0.87.

well. Previous injection studies with `BayesWave` have shown that WNBs can be difficult to reconstruct. One reason is that the WNBs are unpolarized, while `BayesWave` assumes an elliptical polarization. WNBs also just have a very complicated, non-deterministic frequency evolution. An example WNB waveform is shown in Fig. 7, where we can see that there is no clear frequency evolution. Because the chirplets we use have only linearly increasing or decreasing frequency, the chirplet frame struggles to recover the fine details of signal. Thus we expect chirplets will provide the most benefit for signals with fairly smooth time-frequency evolution.

We can also study what we theoretically would expect that matches to be for these injections. For the match given in Eq. 10, we assume that the injected waveform \bar{h} is dependent on parameters $\bar{\lambda}^i$, and the recovered waveform has parameters λ^i . In the high SNR limit, the recovered and true injected parameters should be relatively consistent, or $\Delta\lambda^i = \bar{\lambda}^i - \lambda^i$ is small. Note that in this context the parameters are those of the wavelet/chirplet representation, and not, for example, the masses and spins of the black holes. We can

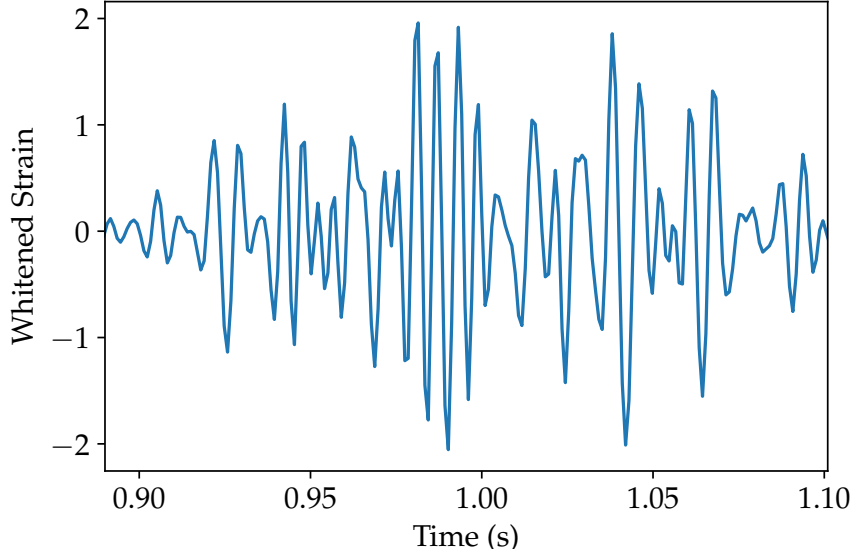


FIG. 7. An example WNB waveform in the time domain. This example waveform shows that WNBs are complicated signals with no well defined frequency evolution.

approximate the recovered waveform as:

$$h = \bar{h} + h_{,i}\Delta\lambda^i \quad (12)$$

and $\Delta\lambda^i$ approximately follows the normal distribution:

$$p(\Delta\lambda^i) = \sqrt{\det(\Gamma/2\pi)} e^{-\Gamma_{ij}\Delta\lambda^i\Delta\lambda^j/2} \quad (13)$$

where $\Gamma_{ij} = (h_{,i}|h_{,j})$ is the Fisher information matrix. We can expand our expression for the match, Eq. 10 then to be [22]

$$M = 1 - \frac{1}{2}\Delta\lambda^i\Delta\lambda^j \left(\frac{(h_{,i}|h_{,j})}{(h|h)} - \frac{(h|h_{,i})(h|h_{,j})}{(h|h)^2} \right). \quad (14)$$

Recognizing that the expected value of $\Delta\lambda^i\Delta\lambda^j$ is $E[\Delta\lambda^i\Delta\lambda^j] \approx \Gamma_{ij}^{-1}$ [23], we find the expected match is:

$$E[M] \approx 1 - \frac{D-1}{2\text{SNR}^2}. \quad (15)$$

where D is the dimension of the model. The minus one comes from the second term in Eq. 14 removing the dependence on the amplitude of the signal. Note that this derivation assumes a templated search, and so should be thought of as more of a “rule of thumb” for this analysis. Using the scaling for the number of wavelets in Eq. 11, we have $D = N_p(\alpha + \gamma\text{SNR}) + 4$, where

N_p is 5 for wavelets, and 6 for chirplets, and an additional 4 common extrinsic parameters (sky location, ellipticity and polarization angle). The full expression for the predicted match is then:

$$E[M] \approx 1 - \frac{N_p(\alpha + \gamma\text{SNR}) + 3}{2\text{SNR}^2}. \quad (16)$$

Figure 8 shows again the average match for the injected binary black hole signals, with the match predicted by Eq. 16. The recovered matches for the BBH injections follow the predicted match relatively well, however the recovered matches for the WNB injections are lower than the analytical prediction due to the signal model (polarized) not matching the simulated signals (un-polarized).

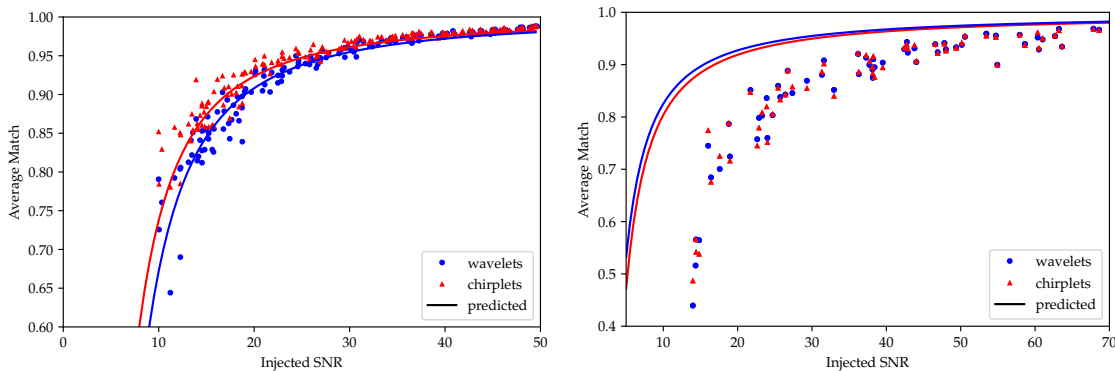


FIG. 8. The predicted match 16 plotted with the actual match for the set of BBH injections (left) and WNB injections (right). The BBH injections generally follow the predicted match vs. SNR scaling, but the prediction overestimates the match for unpolarized WNB injections since the `BayesWave` signal model assumes elliptical polarization.

C. Bayes Factors

The `BayesWave` algorithm considers three distinct models: GW Signals + Gaussian noise (\mathcal{S}); Noise transients (Glitches) + Gaussian noise (\mathcal{G}); Gaussian noise (\mathcal{N}); and computes evidence ratios, or Bayes factors, between the models. Here we investigate how the choice of frame impacts the Bayes factors between the models.

Figure 9 shows $\ln \mathcal{B}_{\mathcal{S},\mathcal{N}}$ (left) and $\ln \mathcal{B}_{\mathcal{S},\mathcal{G}}$ (right) recovered using chirplets and wavelets for simulated binary black hole signals. We see that both bases return very similar $\ln \mathcal{B}_{\mathcal{S},\mathcal{N}}$, with the chirplet frame giving just slightly higher Bayes factors. This is unsurprising since

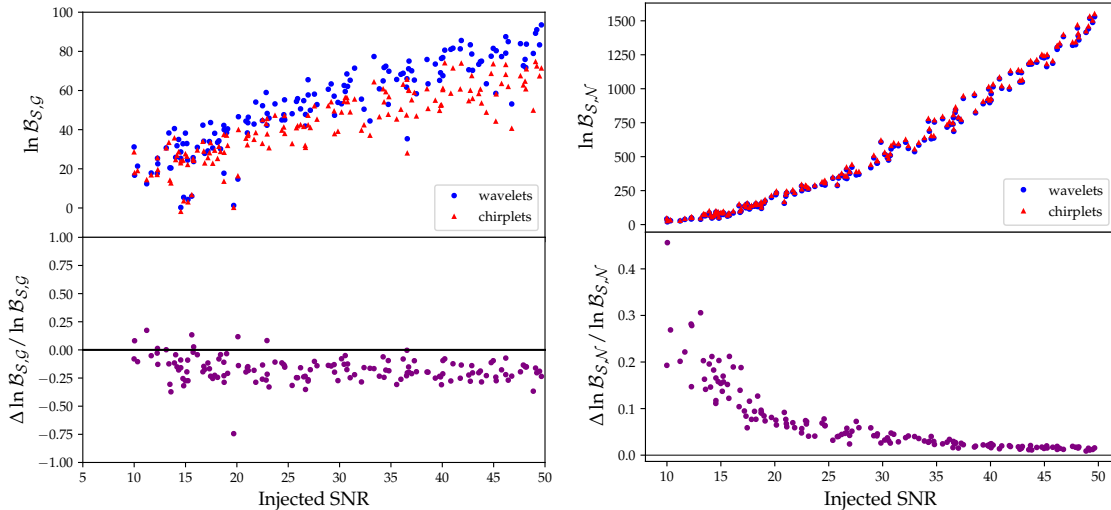


FIG. 9. The log signal-to-glitch (left) and signal-to-noise (right) Bayes factors for a set of $50-50M_{\odot}$ binary black holes using the chirplet and wavelet bases. The lower panel shows the difference in the log Bayes factors between the chirplet and wavelet frames, scaled by the wavelet frame log Bayes factor.

$\ln \mathcal{B}_{S,N}$ scales with the recovered SNR, and chirplets are able to recover more SNR due to their ability to recover signals with higher fidelity.

The signal-to-glitch Bayes factors $\ln \mathcal{B}_{S,G}$ show the opposite behavior, with the wavelet frame providing better separation between signals and glitches than the chirplet frame. This seemingly paradoxical result is due to the chirplet frame providing higher fidelity reconstructions using less parameters for *both* signals *and* glitches. Moreover, since the glitch model sees the signal in the individual detectors, which has lower signal-to-noise than the network response seen by the signal model, and since the chirplets outperform wavelets mostly at low SNR, the chirplet model boosts the evidence for the glitch model more than it boosts the evidence for the signal model, resulting in lower $\ln \mathcal{B}_{S,G}$ than for the wavelet model. From the perspective of a search, where the goal is to separate signals from instrument noise, the wavelet frame outperforms the chirplet frame despite not doing as well at reconstructing signals. The same behavior was also seen when using the “clustering prior” [7], which leads to higher matches, especially at low SNR, but worse separation between signals and glitches.

The reduction in the signal-to-glitch Bayes factor has prevented the clustering prior and the chirplet frame from being used in the current LIGO/Virgo analyses, despite the im-

improvements they offer for signal and glitch reconstruction. We made this decision in order to maximize detection capabilities (i.e. signal and glitch separation), rather than focusing on our waveform reconstruction capabilities. Going forward we plan to implement new models that do a much better job of separating signals and glitches, and that will not penalize models that do a better job of fitting low signal-to-noise features. One option is to modify the glitch model to be anti-coincident between detectors. This can be done by introducing a prior that disfavors placing wavelets at frequencies and times that are occupied by wavelets in the glitch models for the other detectors.

V. DISCUSSION

We have found that added flexibility offered by chirplet frame functions can reduce the overall model dimension, despite adding an additional parameter to each frame function, and improve waveform reconstruction, particularly at low SNRs. Limitations in the model selection approach that is currently used by `BayesWave` to distinguish between signals and glitches has so-far prevented the adoption of chirplets, but these limitations will soon be resolved. Ideally `BayesWave` should utilize a wide range of frame elements, including different types of wavelets and chirplets, and perhaps reduced-basis elements for black hole signals [24]. The optimal mix could then be dynamically selected via the trans-dimensional MCMC algorithm, hewing closer to our mantra “model everything and let the data sort it out”.

VI. ACKNOWLEDGMENTS

MM and NJC appreciate the support of NSF award PHY-1306702. We thank James Clark for his thoughtful comments.

Appendix A: Match

Computing the match as described in Eq. 10 between two chirplets (or wavelets) can be used to further understand how chirplets are represented in time-frequency space. Here we go through this calculation and show how it can be used to derive an expression for the

chirplet ellipse in time-frequency space.

For two *wavelets* the match is given by

$$M = \sqrt{\frac{2\tau_1\tau_2}{\tau_1^2 + \tau_2^2}} \cos\left(\Delta\phi - \frac{2\pi\Delta t_0(f_{01}\tau_1^2 + f_{02}\tau_2^2)}{\tau_1^2 + \tau_2^2}\right) e^{-\frac{\Delta t^2 + \pi^2\tau_1^2\tau_2^2\Delta f_0^2}{\tau_1^2 + \tau_2^2}}, \quad (\text{A1})$$

where we are working in the high- Q limit and thus dropped terms of order e^{-Q^2} relative to the leading term. When the match is maximized over phase the cosine term above goes to one. Introducing the average $\bar{\tau} = \tau_1 + \tau_2$ and difference $\Delta\tau = \tau_1 - \tau_2$ and working to quadratic order in the parameter differences the match is given by

$$M = 1 - \frac{\Delta\tau^2 + 2\Delta t^2 + 2\pi^2\Delta f_0^2\bar{\tau}^2}{4\bar{\tau}^2}. \quad (\text{A2})$$

A similar but slightly more involved calculation for chirplets gives a match of

$$M = 1 - \frac{4\Delta\tau^2 + 8\Delta t^2 + 8\pi^2(\Delta f_0\bar{\tau}^2 - \bar{\beta}\Delta t)^2 + \pi^2(\bar{\tau}\Delta\beta - 2\bar{\beta}\Delta\tau)^2}{16\bar{\tau}^2} \quad (\text{A3})$$

where we are again working to quadratic order in the parameter differences. The full expression of the match, maximized over phase is given by

$$M = \frac{N_1}{D_1^{1/4}} e^{-\frac{N_2}{D_2}} \quad (\text{A4})$$

where

$$N_1 = \sqrt{2\tau_1\tau_2} \left((1 + \pi^2\beta_1^2) (1 + \pi^2\beta_2^2) \right)^{1/4}, \quad (\text{A5})$$

$$D_1 = \pi^6\beta_1^2\beta_2^2(\beta_1\tau_2^2 - \beta_2\tau_1^2)^2 + \pi^4(\beta_1^2\tau_2^2 + \beta_2^2\tau_1^2) - 2\pi^4\beta_1\beta_2(\beta_1\tau_2^2 - \beta_2\tau_1^2)(\beta_1\tau_1^2 - \beta_2\tau_2^2) \\ + \pi^2(\beta_1\tau_1^2 - \beta_2\tau_2^2)^2 + 2\pi^2(\tau_1^2 + \tau_2^2)(\beta_1\tau_2^2 + \beta_2\tau_1^2)^2 + (\tau_1^2 + \tau_2^2)^2, \quad (\text{A6})$$

$$N_2 = ((1 + \pi^2\beta_2^2)\tau_1^2 + (1 + \pi^2\beta_1^2)\tau_2^2)(t_{01} - t_{02})^2 + \pi^2\tau_1^2\tau_2^2(\tau_1^2 + \tau_2^2)(f_{01} - f_{02})^2 \\ - 2\pi^2\tau_1^2\tau_2^2(\beta_1 + \beta_2)(t_{01} - t_{02})(f_{01} - f_{02}). \quad (\text{A7})$$

$$D_2 = (\tau_1^2 + \tau_2^2)^2 + \pi^2(\beta_1\tau_2^2 - \beta_2\tau_1^2)^2. \quad (\text{A8})$$

We further simplify this expression by maximizing over $\Delta\tau$ and $\Delta\beta$, and introducing the dimensionless variables $x = \Delta t/\bar{\tau}$ and $y = \Delta f_0\bar{\tau}$:

$$M_{\max} = 1 - \frac{x^2 + \pi^2(y - \bar{\beta}x)^2}{2}. \quad (\text{A9})$$

The numerator of the second term defines the orientation of the ellipses covered by the chirplets. Thus the angle θ that the ellipse is rotated up from the time axis is given by

$$\tan(2\theta) = \frac{2\pi^2\beta}{\pi^2(1 - \beta^2) - 1}. \quad (\text{A10})$$

-
- [1] B. P. Abbott *et al.* (Virgo, LIGO Scientific), Phys. Rev. Lett. **116**, 131103 (2016), arXiv:1602.03838 [gr-qc].
- [2] B. P. Abbott *et al.* (LIGO Scientific Collaboration and Virgo Collaboration), Phys. Rev. Lett. **116**, 061102 (2016).
- [3] B. P. Abbott *et al.* (Virgo, LIGO Scientific), Phys. Rev. **D95**, 042003 (2017), arXiv:1611.02972 [gr-qc].
- [4] B. P. Abbott *et al.* (Virgo, LIGO Scientific), Phys. Rev. **X6**, 041015 (2016), arXiv:1606.04856 [gr-qc].
- [5] B. P. Abbott *et al.* (Virgo, LIGO Scientific), Phys. Rev. Lett. **116**, 241102 (2016), arXiv:1602.03840 [gr-qc].
- [6] B. P. Abbott *et al.* (Virgo, LIGO Scientific), Phys. Rev. Lett. **116**, 221101 (2016), arXiv:1602.03841 [gr-qc].
- [7] N. J. Cornish and T. B. Littenberg, Classical and Quantum Gravity **32**, 135012 (2015).
- [8] T. B. Littenberg, J. B. Kanner, N. J. Cornish, and M. Millhouse, Phys. Rev. D **94**, 044050 (2016).
- [9] J. B. Kanner, T. B. Littenberg, N. Cornish, M. Millhouse, E. Xhakaj, F. Salemi, M. Drago, G. Vedovato, and S. Klimenko, Phys. Rev. D **93**, 022002 (2016).
- [10] B. Bcsy, P. Raffai, N. J. Cornish, R. Essick, J. Kanner, E. Katsavounidis, T. B. Littenberg, M. Millhouse, and S. Vitale, The Astrophysical Journal **839**, 15 (2017).
- [11] S. Mann and S. Haykin, Vision Interface '91 , 205 (1991), iSSN 0843-803X.
- [12] E. Chassande-Mottin and A. Pai, Phys. Rev. **D73**, 042003 (2006), arXiv:gr-qc/0512137 [gr-qc].
- [13] E. J. Candès, P. R. Charlton, and H. Helgason, Appl. Comput. Harmon. Anal. **24**, 14 (2008), arXiv:gr-qc/0604017 [gr-qc].
- [14] A. Pai, E. Chassande-Mottin, and O. Rabaste, Phys. Rev. **D77**, 062005 (2008), arXiv:0708.3493 [gr-qc].

- [15] E. Chassande-Mottin, M. Miele, S. Mohapatra, and L. Cadonati, *Proceedings, 14th Workshop on Gravitational wave data analysis (GWDAW-14): Rome, Italy, January 26-29, 2010*, Class. Quant. Grav. **27**, 194017 (2010), arXiv:1005.2876 [gr-qc].
- [16] S. Mohapatra, Z. Nemtzow, E. Chassande-Mottin, and L. Cadonati, *Gravitational waves. Numerical relativity - data analysis. Proceedings, 9th Edoardo Amaldi Conference, Amaldi 9, and meeting, NRDA 2011, Cardiff, UK, July 10-15, 2011*, J. Phys. Conf. Ser. **363**, 012031 (2012), arXiv:1111.3621 [gr-qc].
- [17] J. Kovacevic and A. Chebira, Foundations and Trends in Signal Processing **2**, 1 (2008).
- [18] B. P. Abbott *et al.* (VIRGO, LIGO Scientific), (2013), 10.1007/lrr-2016-1, [Living Rev. Rel.19,1(2016)], arXiv:1304.0670 [gr-qc].
- [19] A. Buonanno, Y. Pan, J. G. Baker, J. Centrella, B. J. Kelly, S. T. McWilliams, and J. R. van Meter, Phys. Rev. D **76**, 104049 (2007).
- [20] J. Abadie *et al.* (The LIGO Scientific Collaboration and The Virgo Collaboration), Phys. Rev. D **85**, 122007 (2012).
- [21] M. Maggiore, *Gravitational Waves: Volume 1: Theory and Experiments*, Gravitational Waves (OUP Oxford, 2008).
- [22] B. J. Owen and B. S. Sathyaprakash, Phys. Rev. D **60**, 022002 (1999).
- [23] M. Vallisneri, Phys. Rev. D **77**, 042001 (2008).
- [24] S. E. Field, C. R. Galley, F. Herrmann, J. S. Hesthaven, E. Ochsner, and M. Tiglio, Phys. Rev. Lett. **106**, 221102 (2011), arXiv:1101.3765 [gr-qc].